

# Tension-induced giant actuation in unstructured elastic sheets

Kexin Guo,<sup>1,\*</sup> Marc Suñé,<sup>2,\*</sup> Kwok Ming Li,<sup>1</sup> K. Jimmy Hsia,<sup>1,3,†</sup> Mingchao Liu,<sup>1,4,‡</sup> and Dominic Vella<sup>2,§</sup>

<sup>1</sup>*School of Mechanical and Aerospace Engineering,*

*Nanyang Technological University, Singapore 639798, Singapore*

<sup>2</sup>*Mathematical Institute, University of Oxford, Woodstock Rd, Oxford, OX2 6GG, UK*

<sup>3</sup>*School of Chemistry, Chemical Engineering and Biotechnology,*  
*Nanyang Technological University, Singapore 639798, Singapore*

<sup>4</sup>*Department of Mechanical Engineering, University of Birmingham, Birmingham, B15 2TT, UK*

(Dated: August 27, 2024)

Buckling is normally associated with a compressive load applied to a slender structure; from railway tracks in extreme heat [1] to microtubules in cytoplasm [2], axial compression is relieved by out-of-plane buckling. However, recent studies have demonstrated that tension applied to structured thin sheets leads to transverse motion that may be harnessed for novel applications. For instance, tension in one direction can actuate motion in an orthogonal direction, enabling the creation of kirigami grippers [3], ‘groovy metasheets’ for multi-stable morphing [4], and lateral bending of ribbed sheets [5]. Qualitatively similar behaviour has also been observed in simulations of thermalized graphene sheets [6, 7], where clamping along one edge leads to tilting in the transverse direction. Here, we show that this counter-intuitive behaviour is, in fact, generic for thin sheets that have a relatively low stretching modulus compared to the bending modulus, which allows ‘giant actuation’ with moderate strain. Indeed, transverse buckling can be induced by uni-axial tension even in unstructured elastic sheets, provided that the axial loading is sufficiently close to localized. We therefore refer to this as ‘Tension indUced Giant actuation’ (TUG actuation) and study its properties. We show that TUG actuation occurs because of an efficient transfer of applied tensile load into compression and determine scaling results for the transverse angle as a function of applied strain; our scaling results compare favorably with both experiments and simulations. Our findings suggest that controlled buckling in tension can be utilized in a broader range of materials and structures to give TUG actuation, potentially expanding the scope of its application in material science and engineering.

Buckling in compression is the archetype of elastic instability [8]: when compressed along its longest dimension, a thin structure such as a playing card will buckle out-of-plane accommodating the imposed compression without a significant change of length. Given its ubiquity, it is unsurprising that buckling is used as the simplest ingredient through which to understand the failure of structures from bridges to marine and aerospace structures [9]. However, recently examples have emerged in which an applied tension can lead to a large out-of-plane deformation — the hallmark of buckling. The first examples of this ‘buckling in tension’ required ingenious design of structures [10], but have also emerged in natural systems such as the luxation of human fingers [11].

At the same time, there has been increased interest in mechanical meta-materials [12, 13]: elastic objects with a structure that allows for novel functionality. Several examples of these meta-materials seem to buckle in an orthogonal direction under uni-axial extension, and are shown in Fig. 1a,b. For example, groovy metasheets (Fig. 1a) [4] and kirigami grippers (Fig. 1b) [3] look superficially different but both exhibit significant buckling upon a small axial extension. Similar behaviour can be

seen in other systems too, including the ribbed sheet [5].

As a first clue that this behaviour may not need the careful design that we might first assume, the reader is invited to crumple a piece of paper, open it out again, clamp the centre between thumb and finger and then pull along one axis. As shown in Fig. 1c, this informal experiment suggests a similar phenomenology: the paper tilts perpendicular to the direction of pulling. A more formal version of this phenomenon has also recently been observed in simulations of (thermal) graphene when one edge is clamped [6, 7]. This ubiquity of the tensile buckling in these systems suggests something more fundamental that seems not to have been reported previously, and that hence deserves further investigation. A clue on the key ingredients may be understood by modifying the crumpled paper example just considered: if instead of pulling at the centre with fingers, the crumpled paper is firmly clamped in the hands and pulled. Now no tilting is observed.

This observation motivates only using a localized pulling force. Indeed, similar phenomenology can be observed by taking a uniform sheet and stretching with a small clamped region at the centre (Fig. 1d). (In the case of uniform clamping along the edge, the sheet remains planar (see Fig. A2b) suggesting that this behaviour occurs at much smaller strains than are required to cause global wrinkling [14, 15].) This phenomenology cannot, therefore, be caused by the structure inherent in the examples already discussed (and shown in Fig. 1a-c). We

\* These authors contributed equally.

† [kjhsia@ntu.edu.sg](mailto:kjhsia@ntu.edu.sg)

‡ [m.liu.2@bham.ac.uk](mailto:m.liu.2@bham.ac.uk)

§ [dominic.vella@maths.ox.ac.uk](mailto:dominic.vella@maths.ox.ac.uk)

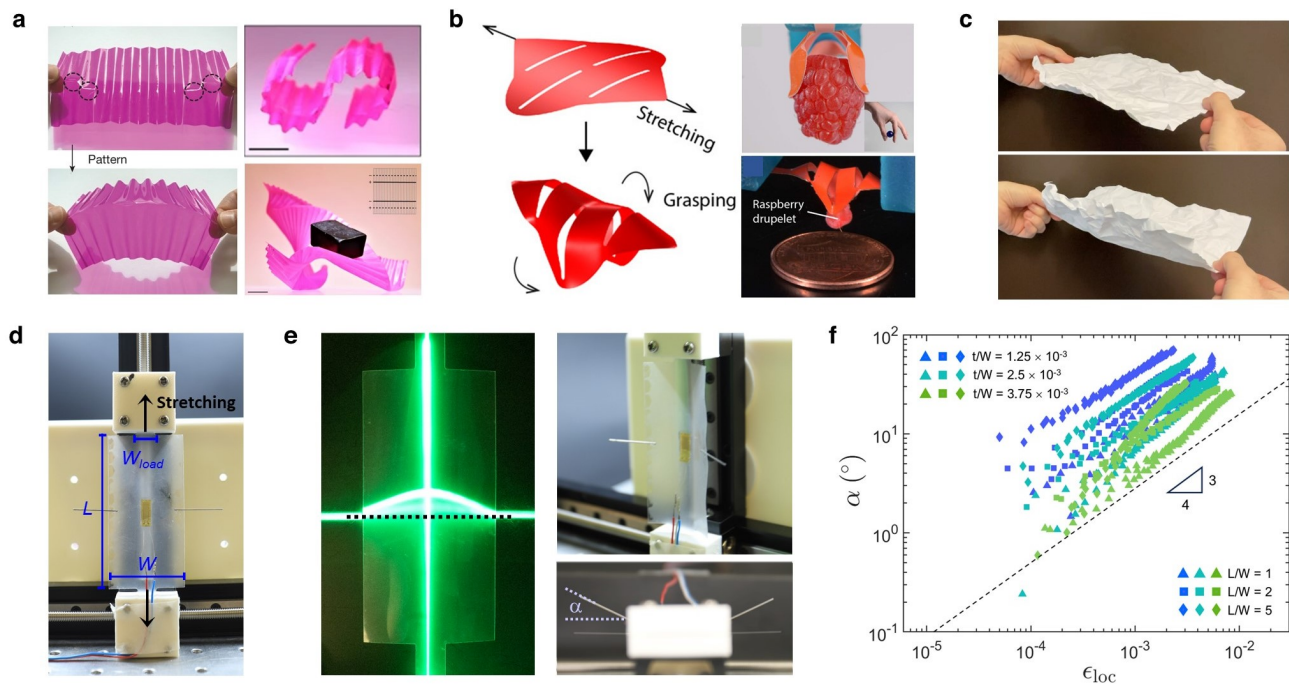


FIG. 1. **Uniaxial, localized tension leads to transverse buckling in a range of structured and unstructured thin sheets.** **a**, A groovy plastic sheet is stretched by point force along the horizontal direction and forms a scar along which the sheet bends and folds (left). Diverse morphologies can be realized (right). Adapted from [4]. **b**, A soft gripper made of a kirigami shell is actuated to grasp a raspberry by stretching along the midline. Adapted from [3]. **c**, A crumpled paper sheet is stretched at the center point along the horizontal direction and demonstrates folding along the transverse direction. **d**, Image showing the experimental setup and associated geometrical parameters of the sheet. **e**, Visualizations of the folding angle,  $\alpha$ , that is observed when the sheet is stretched: left shows the deflection from horizontal of a projected laser line while right shows the deflection of pins attached to the surface which cease being parallel upon deformation. **f**, Experimentally measured folding angles  $\alpha$  as a function of the mean tensile strain,  $\bar{\epsilon}$ , defined in (1). Plotting on a doubly-logarithmic scale for sheets of various dimensions reveals the power-law relationship  $\alpha \propto \bar{\epsilon}^{-3/4}$ , which we seek to explain in this article. For all specimens shown here, we fix  $W_{\text{load}}/W = 0.25$ .

focus thus on experimental realizations in which a small region along the axis is loaded in sheets that are otherwise uniform.

In our experiments, we use rectangular sheets of polyvinyl chloride (PVC) with uniform thickness  $t$  chosen in the range  $40 \mu\text{m} \leq t \leq 150 \mu\text{m}$ ; the sheets were laser cut with length  $L$  and width  $W$  and an additional ‘tab’ (of width  $W_{\text{load}} = 10 \text{ mm}$  and length  $L_{\text{load}} = 30 \text{ mm}$ ) on each side to ensure that a uniform clamping could be applied. The dimensions of the rectangular sheet (excluding the tab) were varied so that  $L \in \{40, 80, 200\} \text{ mm}$  with  $W = 40 \text{ mm}$  was fixed, see Fig. 1f. (These dimensions ensure that the resulting sheet has  $L/W \geq 1$  with  $W/t \gg 1$ .) The Young’s modulus of the PVC used here is given by the manufacturer as  $E = 2 - 4 \text{ GPa}$  (measured by tensile test, as shown in Fig. A1c), though its precise value only scales the forces required to cause a given deformation, not the deformation itself.

The rectangular sheets were clamped by the tabs in 3D-printed fixtures that were attached onto mechanical sliders (Fig. 1d and Fig. A1). They were loaded along the  $y$ -axis by a distance  $\Delta u_y$ . If the sheet remained planar,

this imposed displacement would lead to a planar strain  $\epsilon_{\text{planar}} = \Delta u_y/L$ . However, once the strain reached a small threshold value of  $\epsilon_{\text{planar}}$  (to be discussed in due course) it curls in both  $x$  and  $y$  directions. Figure 1e shows this curving as viewed with laser lines and also with small cannula needles attached to the edge of the sheet; these needles allow us to measure the angle,  $\alpha$ , that the edge of the sheet makes with the horizontal. The evolution of the angle  $\alpha$  with additional strain is shown in Fig. 1f; here the value of the strain is measured using a strain gauge placed at the centre of the sample (see *Methods* for more details). This gives a measure of the local strain  $\epsilon_{\text{loc}}$ .

A plot of the measured inclination angle,  $\alpha$ , as a function of the measured strain,  $\epsilon_{\text{loc}}$ , (see Fig. 1f) shows that  $\alpha \propto \bar{\epsilon}^{-3/4}$ . This scaling is novel in two important respects: firstly, we reiterate that  $\epsilon_{\text{loc}} > 0$  — the sheet is subject to a *tensile* load and yet appears to buckle in the transverse direction. Secondly, this scaling is more sensitive to the imposed end-stretching than the regular (compressive) buckling in which, for example, the amplitude  $A \propto \Delta^{1/2}$  where  $\Delta$  is the imposed end-shortening [16].

To test whether this behaviour is indeed generic, or is caused by some imperfection or anisotropy of the experimental system, we also performed systematic numerical simulations using the finite element method (FEM) software ABAQUS. The results of our FEM simulations are given in Fig. 2, showing the observed inclination angle as a function of the mean strain

$$\bar{\epsilon} = (L' - L)/L, \quad (1)$$

where  $L'$  is the total deformed length. These results demonstrate that the key phenomenology is similar: out-of-plane bending occurs transverse to the imposed stretching (Fig. 2a), while the angle of inclination,  $\alpha$ , follows a power-law similar to that observed experimentally. One important difference between experiments and these numerical simulations is that we observe a small, and  $\bar{\epsilon}$ -independent, angle for very small stretching with a very sudden transition to a larger,  $\bar{\epsilon}$ -dependent,  $\alpha$ , at some critical strain,  $\bar{\epsilon}_c$ . We therefore seek to understand both the emergence of a critical strain,  $\bar{\epsilon}_c$ , and the scaling of the angle  $\alpha$  with  $\bar{\epsilon} > \bar{\epsilon}_c$ .

Our experiments and numerical simulations show a wide range of edge angles  $0.01^\circ \lesssim \alpha \lesssim 100^\circ$  at small imposed strains — the axial strain is at most  $\bar{\epsilon} \sim 10^{-2}$  in Figs. 1 and 2. The conjunction of large out-of-plane deflections and small strains is a common feature of thin sheets and is encapsulated in the Föppl-von Kármán (FvK) plate theory, which combines a mechanically linear response (i.e. a Hookean stress-strain relationship) with nonlinear displacement-strain relationships (i.e. out-of-plane displacements contribute to strains).

The FvK equations therefore couple the stress field within the sheet to the sheet's shape. However, this coupling makes analytical progress difficult. A key simplification comes while the sheet remains planar: we then need only solve for the stress within the loaded sheet. This can be posed as the bi-harmonic equation for the Airy stress function  $\chi$  with appropriate boundary conditions (see Appendix D). The key result of this analysis is that, for sufficiently slender sheets at least, and for  $W_{\text{load}} \ll W$ , the stress components within the sheet remain tensile *except* within a small region close to the edges (i.e. within a typical distance  $W$  from the short edges the transverse stress is compressive). The linearity of this planar problem means that the magnitude of this compressive stress must be linear in the applied tension  $T$ . The coincidence of lengths (i.e. that the lateral scale of the compressed area scales with  $W$ ) and of stresses (i.e. that the resulting transverse compression is linear in the applied tension,  $T$ ) simplifies the near-threshold analysis of instability [17] so that the classic Euler-like buckling analysis is helpful (though see Appendix D for details). Hence, we expect that buckling will occur when  $T$  reaches some multiple of  $B/W^2$ , which immediately gives us that

$$\bar{\epsilon}_c \propto \frac{B}{YW^2}, \quad (2)$$

where  $Y = Et$  is the stretching modulus. For the unstructured, isotropic sheets used here, which have Poisson ratio  $\nu$ ,  $B = Yt^2/[12(1 - \nu^2)]$  and so (2) predicts that

$$\bar{\epsilon}_c \propto \frac{t^2}{(1 - \nu^2)W^2}, \quad (3)$$

which may be interpreted as the reciprocal of the von Kármán number [18]. We shall see later that this prediction is borne out by detailed numerical simulations.

Beyond the buckling threshold, we still impose  $\Delta u_y/L$  but the mean strain  $\bar{\epsilon}$  is not known *a priori*. Since there is additional length in the curved part, we must have that  $\bar{\epsilon} > \Delta u_y/L$ ; we observe in our numerics that for  $\bar{\epsilon} > \bar{\epsilon}_c$  this ‘*excess strain*’ is proportional to  $\bar{\epsilon} - \bar{\epsilon}_c$  (see Appendix C). This gives a first physical understanding of the root of buckling: for  $\bar{\epsilon} < \bar{\epsilon}_c$  the whole planar sheet is subject to significant strain, even though it is not directly loaded (since  $W_{\text{load}}/W \ll 1$ ). Buckling out-of-plane allows a narrow portion of the sheet around the loaded part to accommodate its load, without additionally stretching the unloaded part.

We also observe that the sheet is doubly curved in a narrow region; outside this region, there is a small curvature in the  $y$ -direction (along the pulling direction), while in the  $x$ -direction, the sheet is essentially flat (albeit inclined at the angle  $\alpha$ , see Appendix D). We denote the (unknown) width of this region by  $\omega$ . To determine an estimate for  $\omega$ , we use the experimental (and numerical) observation of the shape to pose as an ansatz for the pulled sheet's shape

$$\zeta(x, y) = \delta \times \begin{cases} \sin \frac{\pi y}{L} \cos \frac{\pi x}{\omega}, & |x| < \omega/2, \\ \frac{\pi}{\omega} \left( \frac{\omega}{2} - |x| \right), & \omega/2 \leq |x| \leq W/2, \end{cases} \quad (4)$$

where  $\delta$  is the maximum amplitude, and the constants have been chosen to ensure that the vertical displacement, slope and curvature of the sheet are all continuous at the edge of the curved central region. Note that this ansatz is only appropriate for  $W_{\text{load}} \ll \omega$ .

The width of the curved region  $\omega$  is not yet known. To determine this, we note that the smaller the value of  $\omega$  the more curved the sheet is in the central region, and the higher its bending energy is:  $U_{\text{bend}} \sim B \int (\nabla^2 \zeta)^2 dA \sim B \delta^2 L / \omega^3$  (where we have neglected the bending energy due to the curvature in the  $y$ -direction because  $L \gtrsim W \gg \omega$ ). Conversely, the excess stretching energy caused by being doubly-curved is localized to this central region so that  $U_{\text{stretch}} \sim \int \sigma : \epsilon dA \sim WLT^2/Y + \omega LT \delta^2/L^2$ , after we make the common assumption that the sheet buckles in the compressing ( $x$ ) direction to relax the compressive stress. Notice also that there are two different length scales for the two terms in  $U_{\text{stretch}}$ : the whole sheet, of width  $W$ , feels the longitudinal tension, but only the narrow strip, of width  $\omega$ , is subject to the additional strain,  $\sim \delta^2/L^2$ , from double-curvature. In the first term in  $U_{\text{stretch}}$  we also assume that  $\Delta u/L \sim T/Y$  remains true after buckling, by virtue of the observation

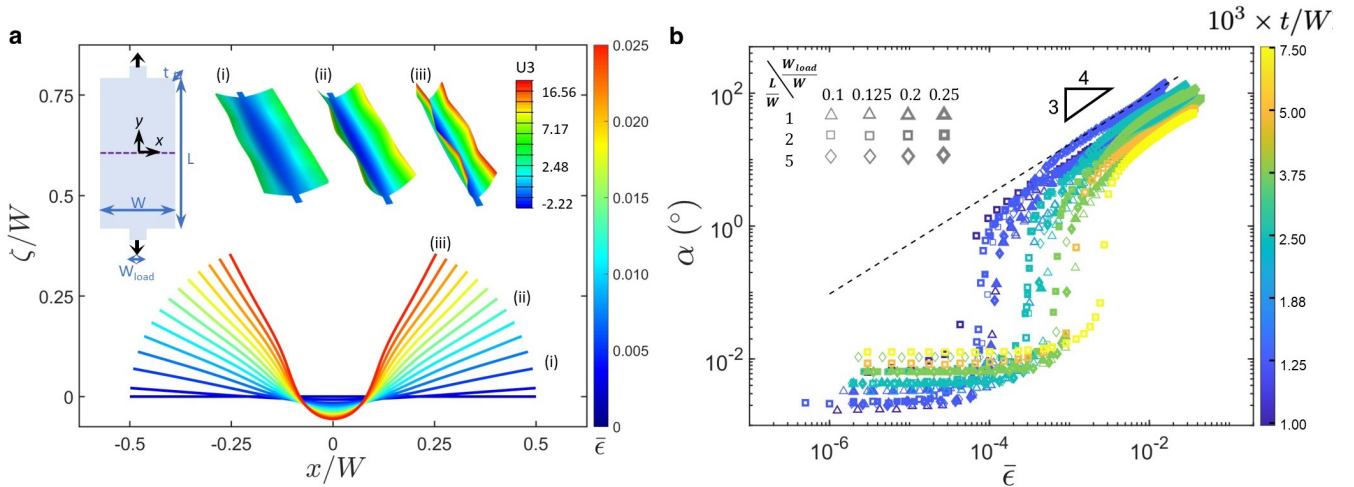


FIG. 2. **Finite element simulations of tensile stretching induced folding in elastic sheets.** **a**, Cross-sectional profiles of a sheet stretched along the  $y$ -axis in normalized units. The color bar indicates the tensile strain of the midline at  $x = 0$  (see top-left inset). The top-right insets (i-iii) show the deformed shapes of the elastic sheet at increasing strains, with colors indicating the  $\zeta$ -displacements according to the color bar for  $U_3$ . The model shown here has the geometry  $L/W = 2$ ,  $t/W = 2.5 \times 10^{-3}$ ,  $W_{\text{load}}/W = 0.1$ . **b**, Simulation results of tensile strains and folding angles for elastic sheets with various geometric parameters. The color bar indicates the thickness-to-width ( $t/W$ ) ratio. The strains and folding angles also display a slope of  $3/4$ , illustrated by the dotted guideline.

that  $\bar{\epsilon} - \Delta u_y/L \propto \bar{\epsilon} - \bar{\epsilon}_c$  sufficiently close to the buckling threshold ( $(\bar{\epsilon} - \bar{\epsilon}_c)/\bar{\epsilon}_c \lesssim 10$ , from Fig. A5b). The total elastic energy,  $U_{\text{bend}} + U_{\text{stretch}}$ , is then minimized when

$$\omega \propto \left( \frac{BL^2}{T} \right)^{1/4} = \left( \frac{BL^2}{Y\bar{\epsilon}} \right)^{1/4}. \quad (5)$$

Note that the scaling law for the width of the curved region, (5), is identical to the scaling for the wavelength of wrinkling observed when a sheet has its whole width clamped and is then pulled perpendicular to this width [15]. We will discuss the similarities and the differences between our results and those of Cerda and Mahadevan [15] (CM) later in the text.

Geometry gives that the inclination angle satisfies  $\alpha \approx \tan \alpha = \pi\delta/\omega$  in which  $\omega$  has been determined (at least to a scaling level) by the previous argument and we assume  $\alpha \ll 1$  for consistency with our use of the FvK formalism; the final part of the puzzle therefore is to determine the maximum amplitude  $\delta$  in (4). We note that the imposed mean strain,  $\bar{\epsilon}$ , is, from the definition (1),  $\bar{\epsilon} = \frac{\Delta u_y}{L} + L^{-1} \int_0^L \frac{1}{2} (\partial\zeta/\partial y)^2 dy$  and, further, that our numerics shows that, even after onset,  $\bar{\epsilon} \propto \Delta u_y/L$ . As a result, we have that  $\delta^2/L^2 \propto \bar{\epsilon} - \bar{\epsilon}_c$  and  $\delta \propto L(\bar{\epsilon} - \bar{\epsilon}_c)^{1/2}$ , which, when combined with the geometrical relationship  $\alpha \approx \pi\delta/\omega$ , gives us that

$$\alpha \propto \delta \left( \frac{Y\bar{\epsilon}}{BL^2} \right)^{1/4} \propto \left( \frac{YL^2}{B} \right)^{1/4} \bar{\epsilon}^{1/4} (\bar{\epsilon} - \bar{\epsilon}_c)^{1/2}. \quad (6)$$

Note that here we have employed an empirical observation, based on our numerics, to understand the scaling of

the amplitude  $\delta$  with strain. Beyond threshold, the non-linear coupling between strain and vertical displacement hinders analytical progress such that even approximate theories based on the FvK framework, e.g. tension field theory (see e.g. the work of Xin and Davidovitch [19] on the CM problem [15]), ultimately require numerical resolution.

To highlight the prediction that  $\alpha \rightarrow 0$  at the critical strain  $\bar{\epsilon}_c$ , we rescale the  $x$ -axis in Fig. 3 on the basis of the predicted scaling for  $\bar{\epsilon}_c$  given in (3); this, in turn, suggests a rescaling for the inclination angle. The results plotted in this way show a reasonable collapse (see Fig. 3); a similar collapse is observed when plotting  $\epsilon_{\text{loc}}$  in the experimental results (see Fig. A4 of the SI).

The prediction for the inclination angle also gives us a more precise means to determine the threshold strain for buckling: except very close to the buckling transition, we expect  $\alpha \propto (\bar{\epsilon} - \bar{\epsilon}_c)^{3/4}$  and so plot  $\alpha^{4/3}$  as a function of  $\bar{\epsilon}$  (see Fig. 4a). This plot shows the expected linear behaviour and also allows us to determine the threshold strain,  $\bar{\epsilon}_c$ , as a function of the sheet thickness ratio,  $t/W$ , and Poisson ratio  $\nu$ . The resulting plot (Fig. 4b) shows that the prediction of (3) is borne out in our numerical simulations, although points with  $L = W$  do not collapse as well as those points with  $L/W \gg 1$ .

Comparing the critical buckling behaviour in our problem (Fig. 4b) and in models of the CM problem (e.g. Fig. 7A in [17]), we note that both have identical scaling behaviour with thickness and width of the sheet (both cases are Euler-like buckling) but find that the threshold value of the dimensionless control parameter  $\bar{\epsilon}_c$  is smaller than  $T_c^{(\text{CM})}/Y$  in the CM problem (see

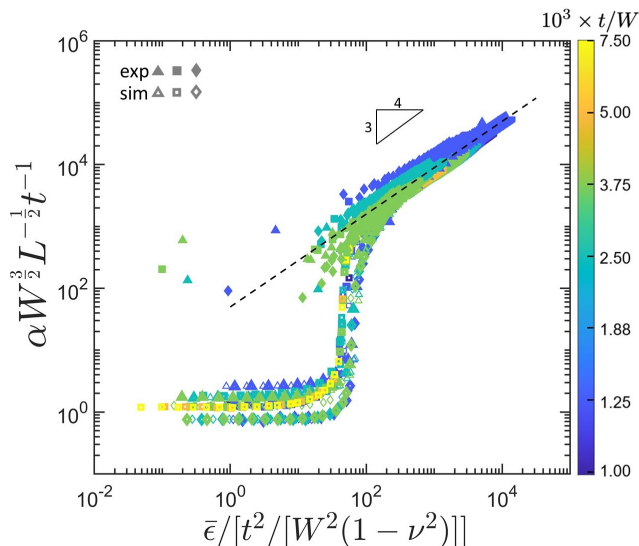


FIG. 3. **Master curve for folding angle,  $\alpha$  ( $^\circ$ ), as a function of mean strain,  $\bar{\epsilon}$ .** Here, results are shown for both simulations and experiments with rescalings suggested by the critical strain at buckling, (3), and the scaling for folding angle (6). (The experimentally measured strain  $\epsilon_{\text{loc}}$  has been converted to an equivalent mean strain based on simulation results — see Fig. A4.)

ref. [17]). In particular, for  $\nu = 0.32$  and  $t/W = 10^{-4}$ , we may write the critical mean strain as

$$\frac{T_c}{Y} \approx \frac{B}{YW^2} \times \begin{cases} 50, & W_{\text{load}} \ll W, \\ 9 \times 10^4 & W_{\text{load}} = W. \end{cases} \quad (7)$$

Note that with the load applied across the full width, the threshold strain required to trigger buckling is more than 1000 times larger than in the localized case considered here. To understand this enhanced resistance to buckling in the CM problem, we compare the maximum compressive stress in the full-width setup (as calculated in ref. [17]) with that in our problem (see Appendix D). For the specific case of  $L/W = 8$  and  $\nu = 0.32$ , we find (data not shown) that

$$\max_y \left\{ \frac{-\sigma_{xx}}{T} \right\} \approx \begin{cases} 0.5, & W_{\text{load}} \ll W, \\ 0.005, & W_{\text{load}} = W. \end{cases} \quad (8)$$

The magnitude of the maximum compressive stress is hence 100 times larger in the localized case considered here than in the full-width case. Recalling that the critical strain was 1000 times larger for the full-width case, we deduce that much of the difference in critical imposed strain can be attributed to the increased efficiency of focusing the longitudinal tensile strain into a transverse compression when pulling at a localized load than at the full-width. However, there also remains an effect of the boundary conditions on the relevant Euler buckling load — indeed, even a standard buckling analysis gives an increase of a factor of 4 between the critical load for

a simply-supported beam (analogous to the freer edges here) and a clamped beam (analogous to the more constrained edges of the CM problem) [20].

We also found that the scaling for the width of the curved region (5) is equivalent to the wavelength of wrinkles in CM [15]. While we emphasize that, for the narrow loading  $W_{\text{load}} \ll \omega$  we studied here, only a single depression is formed (equivalent to half a wavelength), this equivalence suggests that the narrow curved strip is effectively wrinkling around the narrowly loaded part. If we relax the assumption  $W_{\text{load}}/\omega \ll 1$  — by imposing longitudinal strains large enough that  $\omega \sim W_{\text{load}}$ , for example — we observe more wrinkle wavelengths in the curved part of the sheet (data not shown). However, one important difference between the localized-loaded sheet and the fully-clamped sheet is that the latter features fully-developed wrinkle patterns in the small-strain regime.

In conclusion, we have shown that *tensile* loading of an unstructured elastic sheet along one axis actuates motion in an orthogonal direction that is driven by *compression*. A particularly striking feature of this transformation from tension to compression is that it allows a very small strain to actuate a large change in angle: what we might call ‘Tension-indUCed Giant actuation’, or ‘TUG actuation’. We claim that a similar TUG actuation has been observed, if not directly reported, in structured materials — such as a crumpled sheet of paper, kirigami shells [3], and groovy plastic sheets [4] — but to our knowledge has not been reported in regular materials. While the scaling laws we have derived for the critical strain and the inclination angle reveal how the geometry of the sheet and the properties of the material should be tuned to actuate a homogeneous sheet, in the same way, they also give new insights into the mechanisms by which metasheets are able to achieve TUG actuation. Considering the examples of a crumpled sheet of paper, the kirigami grippers [3], and the groovy plastic sheet [4], we note that all involve structures (albeit different in nature) that make stretching in one direction easier while bending in the transverse direction is more difficult. For example, the ridges of a crumpled piece of paper buffer excess length [21] (reducing the effective  $Y$ ), while also increasing the effective thickness (and hence increasing the effective  $B$  [22]), and similarly for the perpendicular cuts and grooves in kirigami grippers and groovy metasheets, respectively. In an unstructured sheet, the combination of a decreased stretching modulus and an increased bending modulus results in an increased buckling strain — see (2). However, at a given multiple of the strain threshold,  $\tilde{\epsilon} = \bar{\epsilon}/\bar{\epsilon}_c$ , this increase in  $B/(YW^2)$  becomes helpful in achieving TUG actuation; in particular, we note that (6) may be rewritten:

$$\alpha \propto \left( \frac{B}{YW^2} \right)^{1/4} \frac{L}{W} \tilde{\epsilon}^{1/4} (\tilde{\epsilon} - 1)^{1/2}, \quad (9)$$

and so, for a given  $\tilde{\epsilon}$ , large  $B/(YW^2)$ , combined with  $L/W \gg 1$ , leads to a large actuation angle. A second key ingredient therefore is the geometrical focusing that

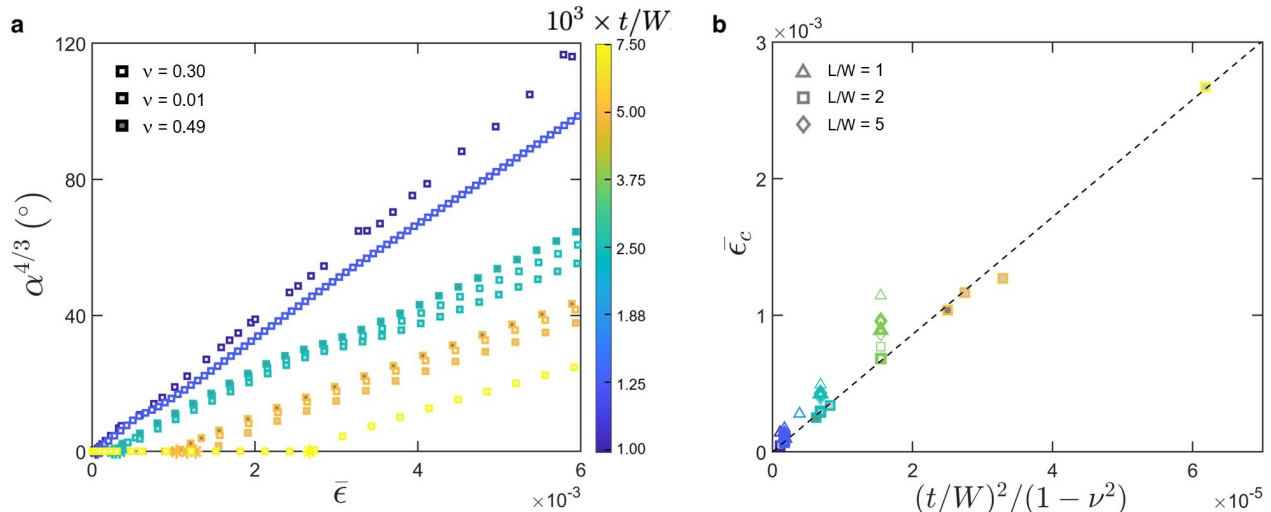


FIG. 4. **Critical buckling behaviour.** **a**, The folding angle  $\alpha$  allows for a clearer determination of the critical strain for wrinkling. The model shown here is the same as in Fig. 2a. **b**, Buckling occurs from where the linear region of the scaled folding angle intersects with the  $x$ -axis, *i.e.*, at critical buckling strains  $\bar{\epsilon}_c$ . The curves shown all have  $L/W = 2$  and  $W_{\text{load}}/W = 0.2$  with various thickness ratios,  $t/W$ , indicated by the color bar. The critical strains for various geometric parameters are linearly related to the ratios  $(t/W)^2$  as shown in the inset.

reduces the critical  $\bar{\epsilon}_c$  by a factor of  $\sim 10^3$  compared to a fully-clamped case (7). The efficiency of this conversion from tension to transverse compression means that a given strain leads to a large  $\alpha$ ; in addition, if  $Y$  is decreased by the structure, such as crumples or cuts, then a fixed load will lead to a still larger strain and hence even larger actuation. This fundamental insight opens the door for designing structures that can more readily demonstrate TUG actuation with or without structure.

#### Acknowledgments

This work was partially supported by the UK Engineering and Physical Sciences Research Council via Grant No. EP/Y027949/1 (MS and DV); the Ministry of Education, Singapore, via MOE AcRF Tier 3 Award MOE-MOET32022-0002 (KJH); the Presidential Postdoctoral Fellowship from Nanyang Technological University, Singapore, and the start-up funding from the University of Birmingham, UK (ML). We thank Ms Mariona Caus for assisting in taking the pictures in Fig. 1c.

#### Methods

*a. Sample preparation* Test specimens were prepared from commercial PVC films with thickness  $t \in \{40, 100, 150\} \mu\text{m}$ . Rectangular sheets were laser cut with width  $W = 40$  mm, length  $L \in \{40, 80, 200\}$  mm, and two tabs with width  $W_{\text{load}} = 10$  mm and length  $L_{\text{load}} = 30$  mm at each end, as shown in Fig. A1b. The fixtures were then attached to the blocks of two linear-stage motors that were controlled manually via the knobs. The specimens were clamped at the tabs in 3D-printed clamp fixtures designed with teeth on the inner

surfaces to reduce slipping. Prior to clamping the specimen, strain gauges (Tokyo Measuring Instruments Laboratory, GFLA-6-350-70) (which have a gauge length of 6 mm, resistance of  $350\Omega$ , and resolution of  $1\mu\epsilon$ ) were adhered to the center of the specimen using strain gauge adhesives (Tokyo Measuring Instruments Laboratory). Strain data measured were recorded by a data logger (Tokyo Measuring Instruments Laboratory, TDS-303). Folding angles of the sheets were measured from photographs taken from the orthogonal plane (Fig. A1d) with the assistance of cannula needles adhered to the edges of the sheet. The needle lines were detected using MATLAB scripts, where the folding angles were measured as the average values of the left and right sides.

*b. Numerical simulations* Numerical simulation was conducted using the commercial finite element analysis software ABAQUS/2023 using S4R shell elements. Linear elastic constitutive relation was applied with Young's modulus  $E = 3000$  MPa and Poisson's ratio  $\nu = 0.3$  (We also varied  $\nu$  from 0.01 to 0.49 for the results in Fig. 4). The boundary conditions were set as in the experiment: the top edge of the upper tab was fully fixed, while displacement loading was applied along  $y$ -axis to the bottom edge of the lower tab. Two analysis steps were conducted in sequence: first, a small out-of-plane displacement were applied to the midline along  $x = 0$  with a magnitude of  $\sim 1\%$  of shell thickness, introducing initial imperfections to the planar shell; second, the static analysis step was performed for the process of tensile stretching and sheet folding.

[1] G. P. Pucillo, "Thermal buckling and post-buckling behaviour of continuous welded rail track," *Int. J. Vehic.*

*Sys. Dyn.* **54**, 1785–1807 (2016).

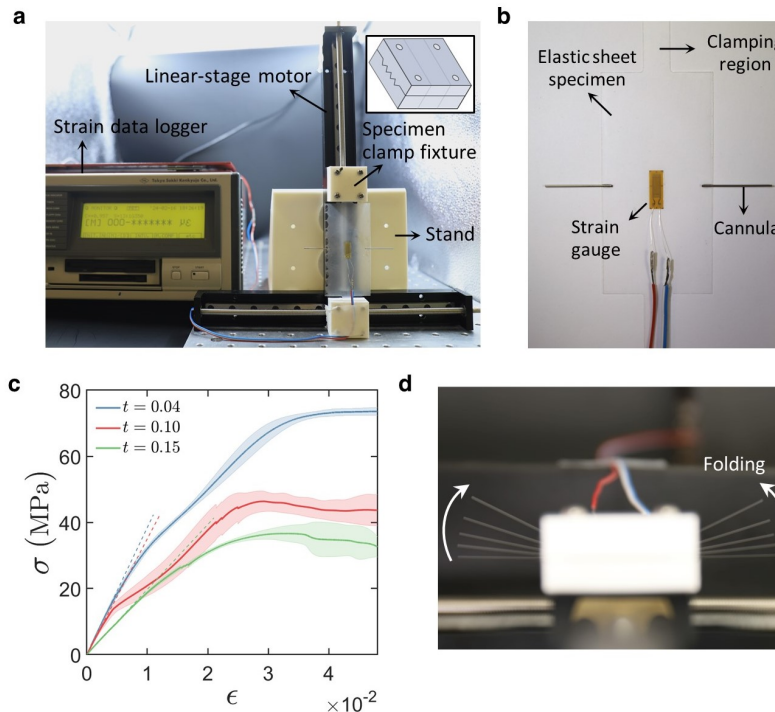
- [2] C. P. Brangwynne, F. C. MacKintosh., S. Kumar, N. A. Geisse, J. Talbot, L. Mahadevan, K. K. Parker, D. E. Ingber, and D. A. Weitz, “Microtubules can bear enhanced compressive loads in living cells because of lateral reinforcement,” *J. Cell Bio.* **173**, 733–741 (2006).
- [3] Y. Yang, K. Vella, and D. P. Holmes, “Grasping with kirigami shells,” *Sci. Robotics* **6**, eabd6426 (2021).
- [4] A.S. Meeussen and M. van Hecke, “Multistable sheets with rewritable patterns for switchable shape-morphing,” *Nature* **621**, 516–520 (2023).
- [5] E. Siéfert, N. Cattaud, E. Reyssat, B. Roman, and J. Bico, “Stretch-induced bending of soft ribbed strips,” *Phys. Rev. Lett.* **127**, 168002 (2021).
- [6] Z. Chen, D. Wan, and M. J. Bowick, “Spontaneous tilt of single-clamped thermal elastic sheets,” *Phys. Rev. Lett.* **128**, 028006 (2022).
- [7] R. A. Valenzuela, P. Hanakata, and M. J. Bowick, “Geometric control of tilt transition dynamics in single-clamped thermalized elastic sheets,” *Phys. Rev. E* **128**, 028006 (2023).
- [8] P. M. Reis, “A perspective on the revival of structural (in) stability with novel opportunities for function: From Buckliphobia to Buckliphilia,” *J. Appl. Mech.* **82**, 111001 (2015).
- [9] Robert Millard Jones, *Buckling of bars, plates, and shells* (Bull Ridge Corporation, 2006).
- [10] D. Zaccaria, D. Bigoni, G. Noselli, and D. Misseroni, “Structures buckling under tensile dead load,” *Proc. R. Soc. A* **467**, 1686–1700 (2011).
- [11] M. Fraldi, S. Palumbo, A. Cutolo, A. R. Carotenuto, and D. Bigoni, “Bimodal buckling governs human fingers’ luxation,” *Proc. Natl Acad. Sci. USA* **120**, e2311637120 (2023).
- [12] Katia Bertoldi, Vincenzo Vitelli, Johan Christensen, and Martin Van Hecke, “Flexible mechanical metamaterials,” *Nature Reviews Materials* **2**, 1–11 (2017).
- [13] Pengcheng Jiao, Jochen Mueller, Jordan R Raney, Xiaoyu Zheng, and Amir H Alavi, “Mechanical metamaterials and beyond,” *Nature Communications* **14**, 6004 (2023).
- [14] E. Cerda, K. Ravi-Chandar, and L. Mahadevan, “Thin films: Wrinkling of an elastic sheet under tension,” *Nature* **419**, 579–580 (2002).
- [15] E. Cerda and L. Mahadevan, “Geometry and physics of wrinkling,” *Phys. Rev. Lett.* **90**, 074302 (2003).
- [16] P. Howell, G. Kozyreff, and J. Ockendon, *Applied Solid Mechanics* (Cambridge University Press, Cambridge, UK, 2008).
- [17] M. Xin and B. Davidovitch, “Stretching Hookean ribbons part I: relative edge extension underlies transverse compression and buckling instability,” *Euro. Phys. J. E* **44**, 92 (2021).
- [18] A. Košmrlj and D. R. Nelson, “Statistical mechanics of thin spherical shells,” *Phys. Rev. X* **7**, 011002 (2017).
- [19] M. Xin and B. Davidovitch, “Stretching Hookean ribbons part II: from buckling instability to far-from-threshold wrinkle pattern,” *Euro. Phys. J. E* **44**, 92 (2021).
- [20] Lev Davidovich Landau and Evgenii Mikhailovich Lifshitz, *Theory of elasticity* (Elsevier, 1986).
- [21] D. Vella, “Buffering by buckling as a route for elastic deformation,” *Nat. Rev. Phys.* **1**, 425–436 (2019).
- [22] A. Košmrlj and D. R. Nelson, “Response of thermalized ribbons to pulling and bending,” *Phys. Rev. B* **93**, 125431 (2017).
- [23] J. P. Benthem, “A Laplace transform method for the solution of semi-infinite and finite strip problems in stress analysis,” *Quart. J. Mech. Appl. Math.* **16**, 413–429 (1963).
- [24] M. L. Williams, “Stress singularities resulting from various boundary conditions in angular corners of plates in extension,” *J. Appl. Mech.* **19**, 526–528 (1952).
- [25] Philip McCord Morse and Herman Feshbach, *Methods of Theoretical Physics*, Vol. Part I (Feshbach Publishing LLC, 1981).

**CONTENTS**

References	6
A. Experimental methods	9
B. Finite element method simulation	9
C. Comparison of different strains in experiments	10
D. Details of Mathematical Modelling	11
1. The planar state	13
2. Benthem's Laplace transform method	15
3. Near-threshold analysis	19

## Appendix A: Experimental methods

The stretching equipment was set up by two linear-stage motors with 300 mm range of motion fixed onto a stand, and two specimen clamp fixtures each attached to the slider module on a linear stage (Fig. A1a). Both the specimen fixtures and the stand were 3D printed (Raise3D FDM Printer) using polylactic acid (PLA). The specimen fixtures were custom designed to fit the modules on the linear stage and the clamp surface were patterned with teeth-like structures to enhance grip (Fig. A1a, inset). The specimens (Fig. A1b) were made of laser-cut commercial polyvinyl chloride (PVC) sheets. Elastic modulus of the sheets were determined from tensile tests of rectangular strips with  $W_{load} = W$ . Averaging five samples for each thickness, we obtain the Young's modulus of PVC sheets with thickness 0.04, 0.10, 0.15 mm to be 3.84, 3.50, 1.96 GPa, respectively (Fig. A1c). The sheets used in the experiment have extended 'tabs' which are regions for clamping with width of  $W_{load} = 10$  mm and  $L_{load} = 30$  mm. The connection between the clamping regions and the main part of the sheets was designed with rounded corners of radius 1 mm to prevent failure due to stress concentration. Tensile strains in the elastic sheets were measured by strain gauges (Tokyo Measuring Instruments Laboratory, GFLA-6-350-70) with gauge length of 6 mm, resistance of  $350 \Omega$ , and resolution of  $1 \mu\epsilon$ . The strain gauges were attached to the center of the specimen along the loading direction using an adhesive, and the gauge leads were connected to electrical wires that input to the strain data logger (Tokyo Measuring Instruments Laboratory, TDS-303). When clamping specimens between fixtures, vertical alignment is ensured for symmetric loading. Cannula needles with an outer diameter of  $700 \mu\text{m}$  were adhered to the  $y$ -middle of the sheet near the edges as an indicator in the measurement of folding angles. Photographs were taken from top-view of the specimens during the loading process (Figs. 3e and A1d), from which folding angles were measured using MATLAB.

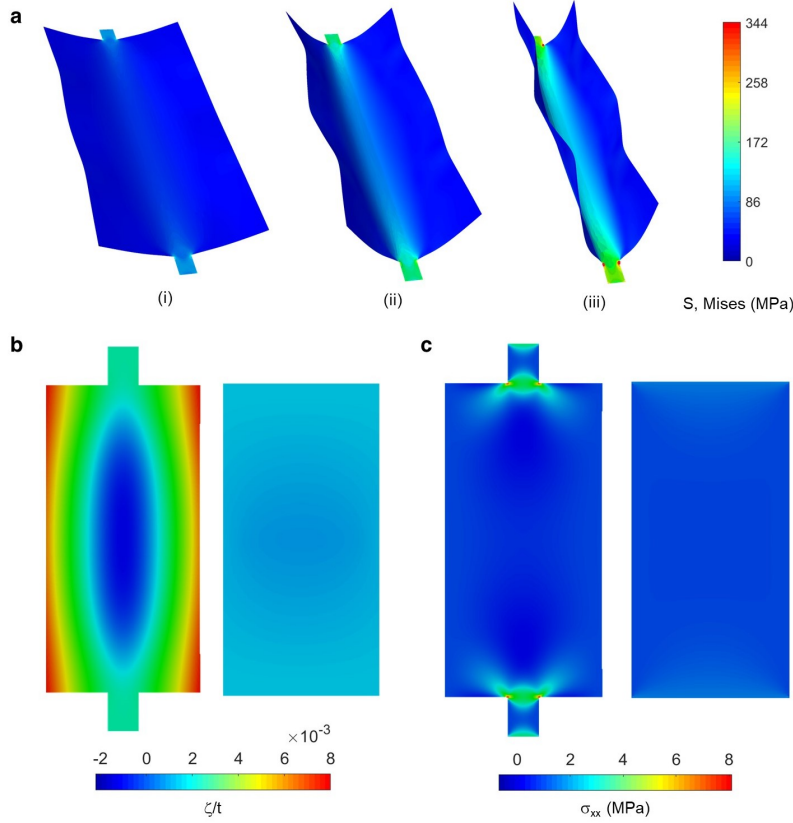


Extended Data Fig. A1. **Experimental setups.** **a**, Tensile-stretching equipment consisting of linear-stage motors, 3D-printed specimen clamp fixtures and a stand (all labelled on the figure). **b**, Testing specimen, showing the location of the strain gauge, cannula and where the sheet is clamped (see labels). **c**, Stress-strain curves of the PVC sheet with fully clamped edge. **d**, Composite image showing the evolution of the folding angle,  $\alpha$ , with increasing strain.

## Appendix B: Finite element method simulation

Numerical simulation was conducted using the commercial finite element analysis software ABAQUS/2023. The model was constructed in 3D space using 2D shell sections and S4R elements. Linear elastic constitutive relation was applied with Young's modulus  $E=3000$  MPa and Poisson's ratio  $\nu=0.3$ . Displacement loading  $U_2$  was applied to the

bottom edge of the lower clamping region, while the top edge of the upper clamping region was fixed in all degrees of freedom. Two analysis steps were conducted in sequence: first, a small out-of-plane displacement to the midline at  $x = 0$  of a magnitude of  $\sim 1\%$  of shell thickness, creating initial perturbation to the planar shell; second, the static analysis step was performed for the process of tensile-stretching induced folding of the elastic sheet.



Extended Data Fig. A2. **FE simulation results.** **a**, Von-Mises stress distributions in stretched sheets in Fig. 2a insets (i-iii). **b-c**, Out-of-plane deflections  $\zeta$  normalized by thickness  $t$  (**b**) and transverse stress  $\sigma_{xx}$  (**c**) in stretched sheets  $L/W = 2, t/W = 0.005$  with partially clamped edges  $W_{\text{load}}/W = 0.2$  (left) and fully clamped edges  $W_{\text{load}}/W = 1$  (right). Contours shown in **b-c** are at the critical buckling strain for the partially clamped case, *i.e.*,  $\bar{\epsilon}_c \approx 1.2 \times 10^{-3}$ .

### Appendix C: Comparison of different strains in experiments

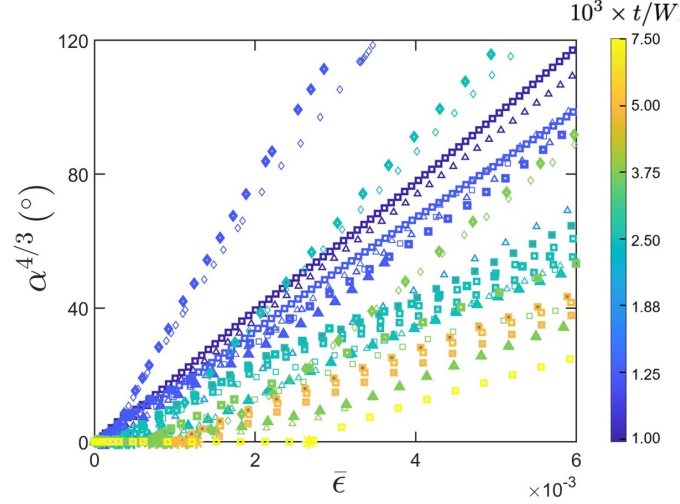
These numerical results allow us to compare the various types of strain that are measured experimentally.

*a. Local to mean strain* Firstly, our experiments measured the local strain,  $\epsilon_{\text{loc}}$ , at the centre of the sheet. This can be converted to an effective mean strain,  $\bar{\epsilon}_{\text{eff}}$ , using numerical results, see Fig. A4a. However, even without this conversion, the comparison between experiments and numerical results, see Fig. A4b is favourable.

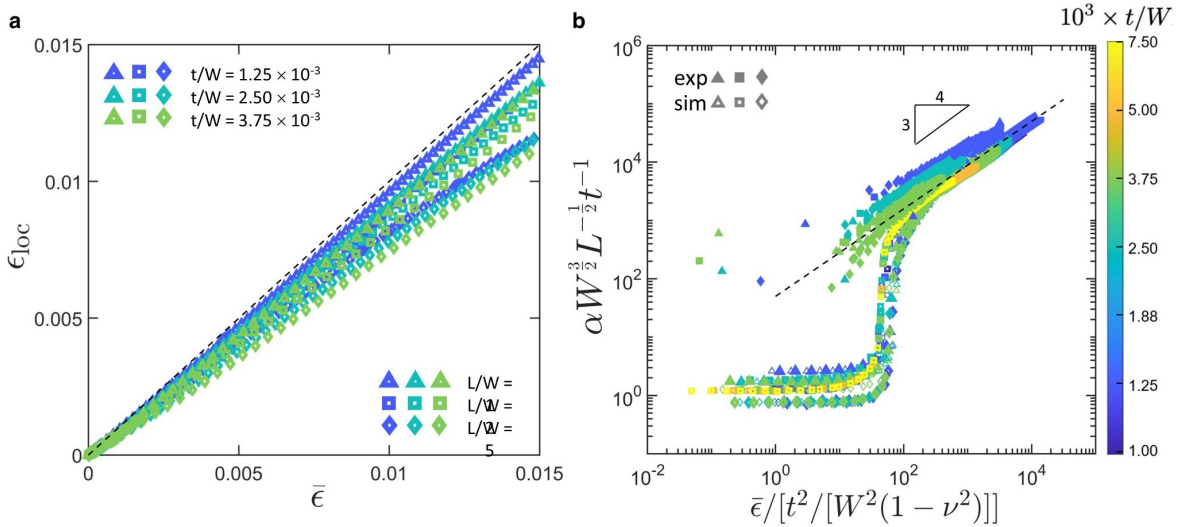
*b. Mean strain versus imposed displacement* Prior to buckling, the mean strain  $\bar{\epsilon} = \Delta u_y/L$ . However, after buckling, this relationship no longer holds. We therefore use numerical simulations to compute the relationship between the two: see Fig. A5a. In Fig. A5b we show see that the discrepancy between the two grows linearly above the buckling threshold, so that:

$$\bar{\epsilon} - \frac{\Delta u_y}{L} = \begin{cases} 0, & \frac{\Delta u_y}{L} < \bar{\epsilon}_c, \\ k \left( \frac{\Delta u_y}{L} - \bar{\epsilon}_c \right), & \frac{\Delta u_y}{L} > \bar{\epsilon}_c. \end{cases} \quad (\text{A1})$$

Crucially, this means we can interchangeably use  $\bar{\epsilon} - \bar{\epsilon}_c$  or  $\Delta u_y/L - \bar{\epsilon}_c$  in scaling and experimental analyses. (Note, however, that the collapse of data is less satisfactory in the case  $L = W$ , for which the sheets are not particularly slender.)



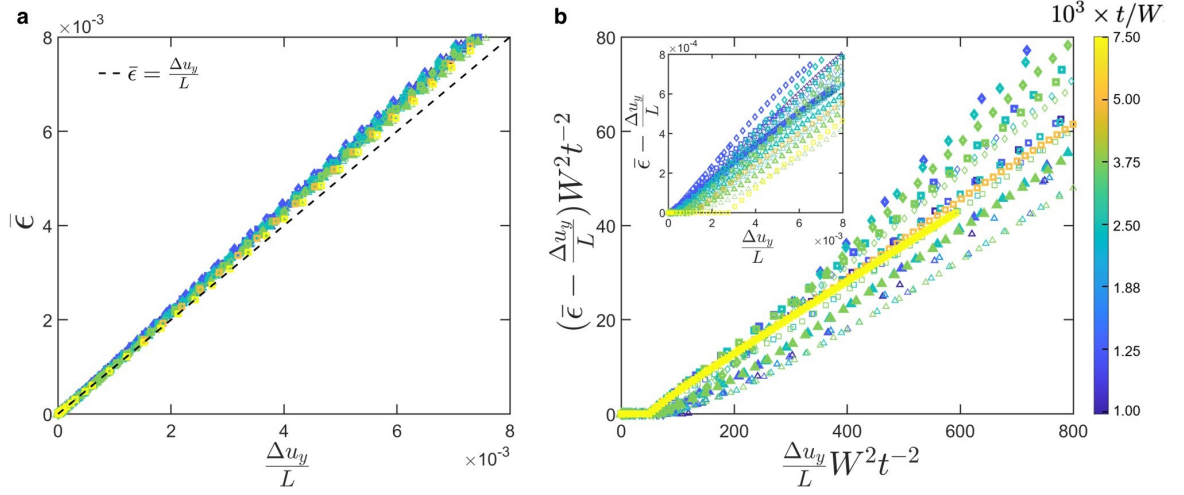
Extended Data Fig. A3. The scaled folding angle exhibits an intersection with the  $x$ -axis prior to the linear region, from where we determine the critical buckling strains  $\bar{\epsilon}$  in Fig. 4b. They have varying  $L/W$ ,  $W_{\text{load}}/W$ , following the legends in Fig. 2b, and  $t/W$  indicated by the color bar.



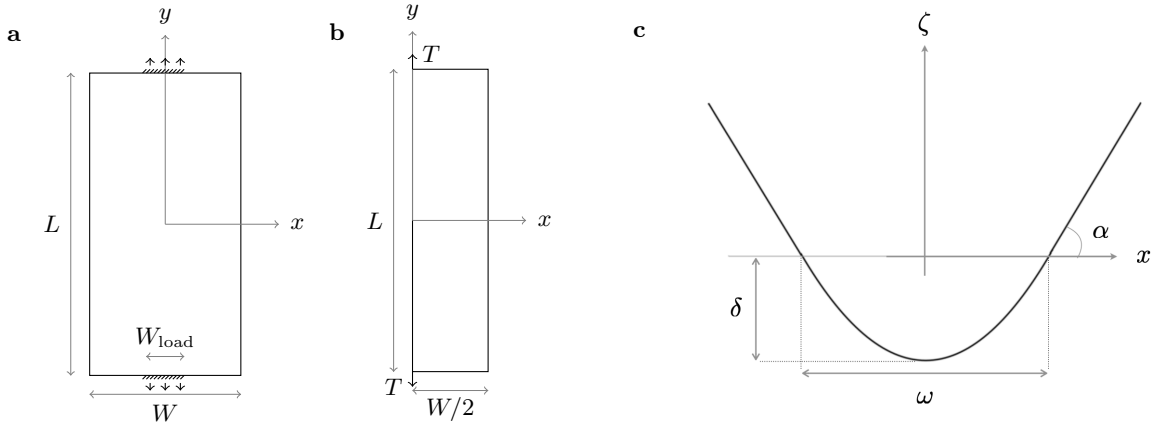
Extended Data Fig. A4. **a**, The strain measured locally at the middle of the sheet,  $\epsilon_{\text{loc}}$ , over a longitudinal length of  $l_{\text{loc}}/W = 0.25$  is smaller than the mean strain within the sheet,  $\bar{\epsilon}$ , but remains an approximately linear function of the strain. In all cases shown  $L/W = 2$  and  $W_{\text{load}}/W = 0.25$ . These parameters correspond to those used in the experiments. In the main text this relationship is used to convert the value of  $\epsilon_{\text{loc}}$  measured experimentally to an effective mean strain  $\bar{\epsilon}_{\text{eff}}$  for plotting in Fig. 3. Without this conversion, the comparison between experimental and numerical results is slightly worse as shown in **b**.

#### Appendix D: Details of Mathematical Modelling

We consider an unstructured thin elastic sheet of thickness  $t$ , width  $W$ , and length  $L$  ( $t \ll W < L$ ) made of a material with Young's modulus  $E$  and Poisson's ratio  $\nu$ . The sheet is clamped in a central segment along the short edges, of width  $W_{\text{load}}$ , and subjected to an in-plane longitudinal stretching strain  $\epsilon_{yy}$  — we choose the long edges to be parallel to the  $y$ -axis. Outside the clamps (*i.e.* for  $|x| > W_{\text{load}}/2$ ), the short edges are free, as well as the long edges (see Fig. A6a). We adopt the Föppl-von-Kármán (FvK) plate theory to model our sheet. We start by introducing the physical quantities that we will use. According to the FvK framework, we linearize the in-plane displacement-strain



Extended Data Fig. A5. **a**, Mean strain, as measured from the arc-length,  $\bar{\epsilon}$  is larger than the directly imposed strain  $\Delta u_y/L$  in the post-buckling regime. **b** Up to the point of buckling  $\bar{\epsilon} = \Delta u_y/L$ , but even after buckling there is a linear relationship, as summarized in (A1). Here the data are scaled so that all data sets pass through the buckling point,  $(\bar{\epsilon}_c t^2/W^2, 0)$ ; the inset shows the data before scaling.



Extended Data Fig. A6. **Schematic diagrams.** **a**, A rectangular sheet, of width  $W$  and length  $L$ , clamped a width  $W_{\text{load}} < W$  along its width. The sheet is longitudinally loaded at the clamps. **b**, A rectangular sheet, of width  $W/2$  and length  $L$ , with localized load  $T$  applied longitudinally at the corners  $(0, \pm L/2)$ . The sheet is transversely clamped at  $(0, y)$ . **c**, A cross-sectional profile (at  $y = 0$ ) of the sheet stretched along the  $y$ -axis by a localized load beyond buckling. The origin in the  $\zeta$ -axis corresponds to the reference plane of the planar solution.

relationship:

$$\begin{aligned} \epsilon_{xx} &= u_{x,x} + \frac{1}{2}(\zeta_{,x})^2; \quad \epsilon_{yy} = u_{y,y} + \frac{1}{2}(\zeta_{,y})^2, \\ \epsilon_{xy} &= \frac{1}{2}(u_{y,x} + u_{x,y} + \zeta_{,x}\zeta_{,y}), \end{aligned} \quad (\text{A1})$$

where  $u_x$ ,  $u_y$  are in-plane components of the displacement field, whose out-of-plane component is  $\zeta$  (we use the comma notation in the subindex to denote the derivatives). We also invoke the two-dimensional Hookean constitutive relations, which link the in-plane strain to the in-plane stress  $(\sigma_{\alpha\beta})$ , which denotes the stress averaged across the sheet

thickness):

$$\begin{aligned}\sigma_{xx} &= \frac{1}{1-\nu^2} Y (\epsilon_{xx} + \nu \epsilon_{yy}), \\ \sigma_{yy} &= \frac{1}{1-\nu^2} Y (\epsilon_{yy} + \nu \epsilon_{xx}), \\ \sigma_{xy} &= \frac{1}{1+\nu} Y \epsilon_{xy},\end{aligned}\tag{A2}$$

where  $Y = Et$  is the stretching modulus. Note that here the  $2d$ -stresses have dimensions of a tension (force  $\times$  length $^{-1}$ ) — in FvK, the in-plane stresses averaged across the thickness are  $t \times \sigma_{\alpha\beta}(z=0)$ .

We consider the limit of small  $W_{\text{load}}$ ,  $W_{\text{load}}/W \ll 1$ . Exploiting the symmetry along the  $x$ -axis, that we align with the short edge, we consider one half of this sheet, *i.e.* a flat sheet of width  $W/2$  and length  $L$  (see Fig. A6b). We examine next the instability of this sheet through a near-threshold analysis [17] of the planar state (*i.e.*  $\zeta = 0$ ). For the beyond threshold analysis, whose main parameters are represented in Fig. A6c, see the main text.

### 1. The planar state

The FvK equations that set the mechanical equilibrium in the planar state reduce to a single bi-harmonic equation:

$$\nabla^4 \chi(x, y) = 0,\tag{A3}$$

after we eliminate the in-plane components of the stress tensor in favour of a single scalar function, the Airy potential  $\chi(x, y)$ , defined as

$$\sigma_{xx} = \chi_{,yy}; \quad \sigma_{yy} = \chi_{,xx}; \quad \sigma_{xy} = -\chi_{,xy}.\tag{A4}$$

We consider only small strains, and hence we assume the boundary conditions (BCs) to apply at the edges  $x = 0, W/2$  and  $y = \pm L/2$ . For convenience, we set the length  $L = 2$  and rescale  $x, y$  with  $L/2$ . The set of BCs for the stress and the displacement fields is then:

$$\text{at } y = \pm 1: \quad \sigma_{yy} = \sigma_{xy} = 0,\tag{A5a}$$

$$\text{at } x = W/2: \quad \sigma_{xx} = \sigma_{xy} = 0,\tag{A5b}$$

$$\text{at } x = 0: \quad u_x = 0, \quad u_{y,y} = \epsilon_{\text{planar}},\tag{A5c}$$

which describes a sheet whose edge at  $x = 0$  is both transversely clamped ( $u_x(x=0) = 0$ ) and longitudinally strained ( $\epsilon_{yy}(x=0) = u_y/L \equiv \epsilon_{\text{planar}} > 0$ ). The edges at  $x = W/2$  and  $y = \pm 1$  are free.

We scale the stresses by the tension  $T = \epsilon_{\text{planar}} Y$ ,  $\sigma_{\alpha\beta}/T$ , and we convert the set of BCs (A5) into BCs for the Airy potential invoking Eq. (A4):

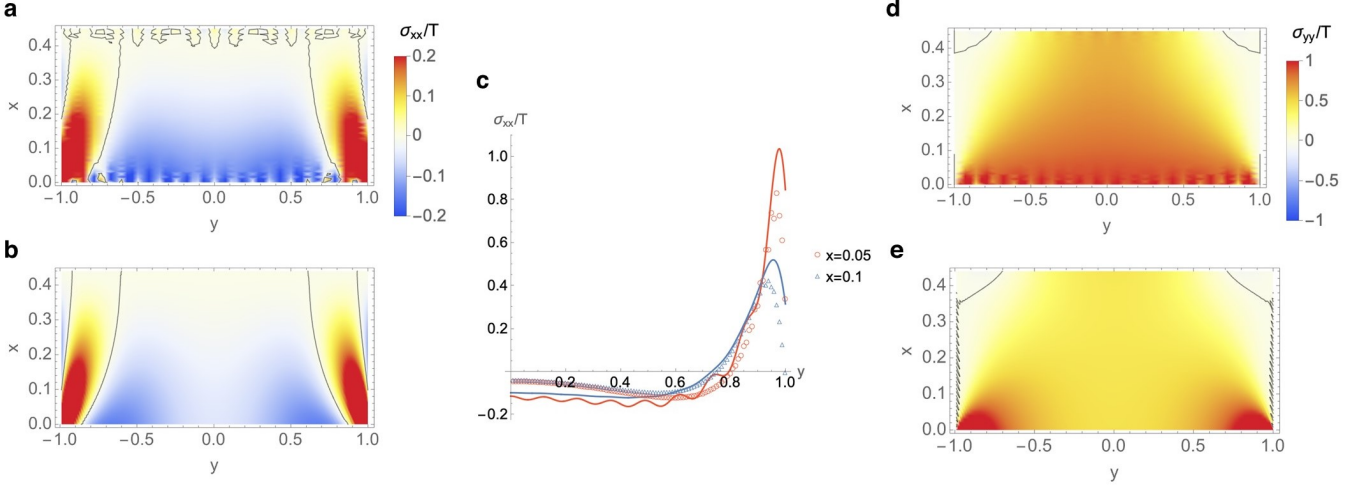
$$\text{at } y = \pm 1: \quad \chi = 0 \quad \text{and} \quad \chi_{,y} = 0,\tag{A6a}$$

$$\text{at } x = W/2: \quad \chi = 0 \quad \text{and} \quad \chi_{,x} = 0,\tag{A6b}$$

$$\text{at } x = 0: \quad \chi_{,xx} - \chi_{,yy}\nu = 1 \quad \text{and} \quad \chi_{,xxx} + (2 + \nu)\chi_{,xyy} = 0.\tag{A6c}$$

Note that we do not introduce any different notation for the scaled stresses  $\sigma_{\alpha\beta}$ , nor for the corresponding Airy potential  $\chi$ . Both equations in (A6a) and (A6b) follow from choosing the natural gauge of vanishing constants of integration when we integrate respectively the first equation in (A4) at  $y = \pm 1$  and the second at  $x = W/2$ . This gauge is consistent with the BCs for the off-diagonal stress components at the free edges  $y = \pm 1$  and  $x = W/2$ .

By virtue of the small strains approximation, *viz.* (A1), the second BC in (A5c) implies that  $\epsilon_{yy}(x=0) = \epsilon_{\text{planar}}$ . Invoking the inverse of the Hookean constitutive relations (A2), and using the definition of the Airy potential (A4), the second BC in (A5c) converts into the first equation in (A6c). Finally, to obtain the last BC in (A6c) we use the off-diagonal strain,  $\epsilon_{yx} = \sigma_{yx}(1 + \nu)/Y$  by inverting the last relation in (A2), which evaluates to  $\epsilon_{yx} = u_{y,x}/2$  at the edge  $x = 0$  after we apply the BCs (A5c) into (A1). Thus, we have  $u_{y,x}/2 = \sigma_{yx}(1 + \nu)/Y$ . Writing this equation in terms of the Airy potential (A4), and taking its  $y$  derivative yields the equation  $u_{y,xy} = -\chi_{,yyy} 2(1 - \nu)/Y$  for the  $x, y$  derivative of the longitudinal displacement. The latter can be obtained from the  $x$  derivative of  $\epsilon_{yy}$ :  $u_{y,xy} = \epsilon_{yy,x} = (\chi_{,xxx} - \nu \chi_{,yyy})/Y$ . The second equation in (A6c) then follows from eliminating  $u_{y,xy}$  from the last two equations.



Extended Data Fig. A7. **Stress in the planar state.** **a**, Analytic solution for the transverse stress (A9a) within the sheet subjected to a longitudinal localized load at the corners as per Fig. A6b;  $W/L = 0.45$  and we take  $n = 16$  terms in the series. **b**, Numeric results for the transverse stress obtained by finite-element simulations (see Appendix B) of a sheet ( $L/W = 2$ ,  $t/W = 0.0025$ ,  $W_{\text{load}}/W = 0.1$ ,  $E = 3000$  MPa,  $\nu = 0.3$ ) subjected to a longitudinal strain  $u_y/L = 0.025$ . The numeric results are rescaled according to the scaling in the mathematical model, and they are only shown within  $x \geq W_{\text{load}}/2$ . The same colorbar as in **a** applies. **c**, Cross-sectional profiles of the transverse stress at different values of  $x$ ; symbols for the numerics, lines for the analytic expression. **d**, Longitudinal component of the stress (A9b). **e**, Numeric results for the longitudinal stress with the same colorbar as in **d**.

We solve the bi-harmonic equation (A3) for the Airy potential with the set of BCs (A6) following the calculation of Benthem [23] (further details on the method are given in Sec. D2):

$$\chi(x, y) = \text{Re} \left[ \sum_k \left\{ C_k e^{p_k(x-W/2)} + \hat{C}_k e^{-p_k x} \right\} \left\{ \cos(p_k y) - (\cot p_k) y \sin(p_k y) \right\} \right], \quad (\text{A7})$$

where  $C_k, \hat{C}_k$  are constants given in (A26) in Sec. D2, and  $p_k$  are the (complex) roots of the trigonometric equation

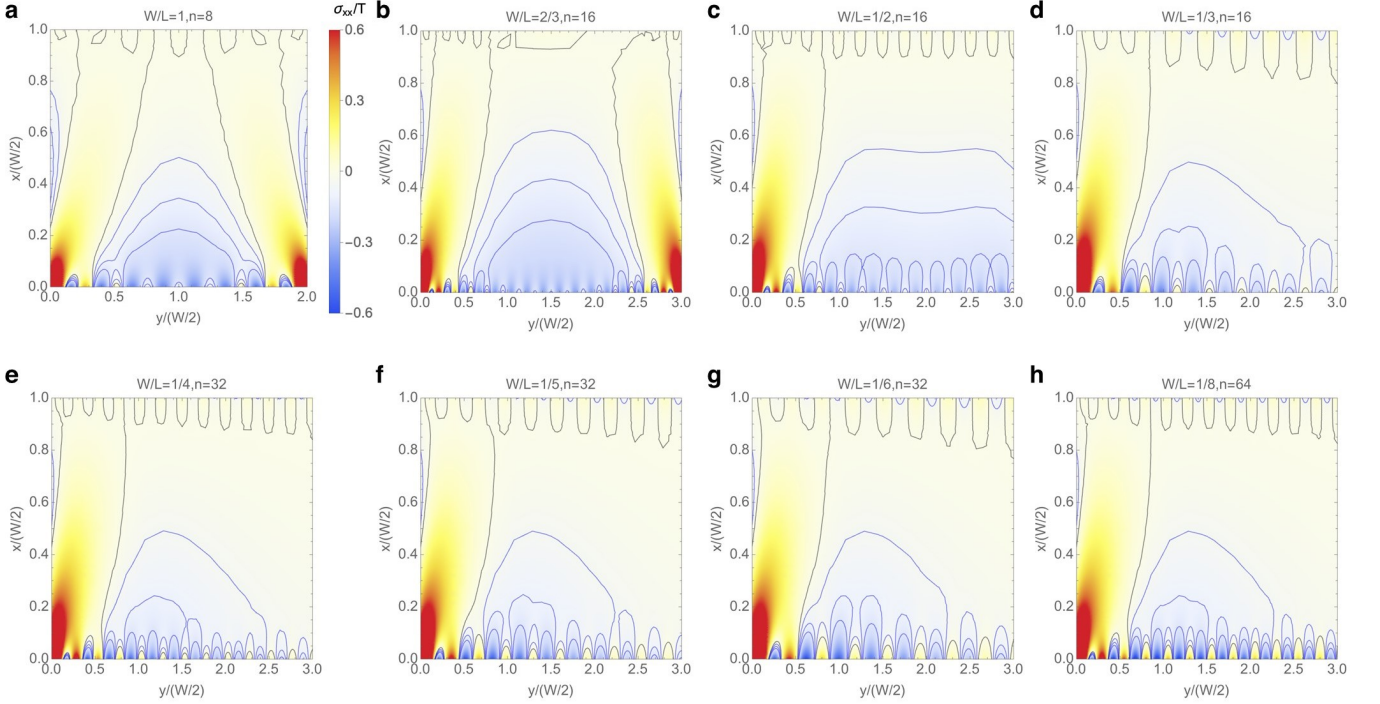
$$\sin 2p_k + 2p_k = 0, \quad (\text{A8})$$

ordered by increasing  $|p_k|$ . We derive the Airy potential and we obtain the transverse and longitudinal components of the stress tensor (A4):

$$\sigma_{xx} = \chi_{,yy} = \text{Re} \left[ \sum_k \left\{ C_k e^{p_k(x-W/2)} + \hat{C}_k e^{-p_k x} \right\} \left\{ -(p_k^2 + 2p_k \cot p_k) \cos(p_k y) + \cot p_k y \sin(p_k y) \right\} \right], \quad (\text{A9a})$$

$$\sigma_{yy} = \chi_{,xx} = \text{Re} \left[ \sum_k (p_k)^2 \left\{ C_k e^{p_k(x-W/2)} + \hat{C}_k e^{-p_k x} \right\} \left\{ \cos(p_k y) - (\cot p_k) y \sin(p_k y) \right\} \right]. \quad (\text{A9b})$$

We benchmark the expressions for the stress in the planar state (A9) with the finite-element simulations (see Appendix B) of a sheet ( $L/W = 2$ ,  $t/W = 0.0025$ ,  $W_{\text{load}}/W = 0.1$ ,  $E = 3000$  MPa,  $\nu = 0.3$ ) subjected to longitudinal strain  $u_y/L = 0.025$ . Considering the scaling assumed previously (*i.e.* lengths are rescaled by  $L/2$  and  $L = 2$ , and stresses are normalized by  $T = Y u_y/L$ ), we plot in Fig. A7 the planar stress state obtained by (A9) and the numerical simulations (for which we consider only the region  $x \geq W_{\text{load}}/2$ ). We notice a good agreement between the analytic calculations (Fig. A7a and d) and the numerics (Fig. A7b and e). The transverse stress (Fig. A7a and b) is tensile at the corners where we exert  $T$ , and compressive as we move away from the corners towards the centre — we have included the contour line at  $\sigma_{xx}/T = 0$  to evince the coexistence of compressive and tensile areas in the sheet. At a distance close to the  $y$ -axis, the cross-sectional profiles of this stress component (Fig. A7c) help us visualize the tension-to-compression transition as we move away from the corners, and the stress singularity at their vicinity (see the next section for more details on the stress singularities at the corners of a sheet). Away from the  $y$ -axis, the transverse stress within the sheet fades rapidly. Conversely, the longitudinal stress (Fig. A7d and e) is tensile everywhere in the sheet, and hence deserves less attention in our discussion.



Extended Data Fig. A8. **Transverse stress in the planar state for different aspect ratios.** **a-h**, Density plots of the stress by the expression (A9a). The longitudinal coordinate,  $y$ , is shifted  $y \rightarrow y + 1$ ; and both axes by  $W/2$ . The same colorbar (only shown in **a**) applies to all panels. The number of terms,  $n$ , taken in the series (A9a) is labeled in each graph. Contour lines are displayed at  $\sigma_{xx}/T = (0, -0.05, -0.1, -0.15)$ .

We further examine the transverse stress for different values of the aspect ratio  $W/L$ . We already noticed that the transverse stresses are weak away from the corners of the sheet that are loaded. Thus, we focus on the stress state close to the loaded corners. We plot in Fig. A8 the expression (A9a) shifted in  $y$ ,  $y \rightarrow y + 1$ , and we scale both axes by  $W/2$ . We observe a universal stress state for  $W/L \lesssim 1/4$ : the transverse stress is tensile at the vicinity of the corner, and compressive within an area that borders the narrow tensile part. The width of this compressing sector scales with  $\sim W$  — we have included contour lines every  $\Delta\sigma_{xx} = -0.05$  in the compressive part so as to evince the behaviour of these stresses. This scaling is paramount in our analysis in the main text. For  $W/L \gtrsim 1/4$ , the compressive sectors corresponding to both corners overlap, and hence the sheet has a single compressed area spanning the centre of the sheet, while the two tensile sectors prevail at the corners.

## 2. Benthem's Laplace transform method

We define the function  $f(x, p)$  as the Laplace transformation of the Airy potential,

$$f(y, p) = \int_0^{W/2} \chi(x, y) e^{-px} dx, \quad (\text{A10})$$

and the subsequent inverse formula

$$\chi(x, y) = \frac{1}{2\pi i} \int_{c-i\infty}^{c+i\infty} f(y, p) e^{px} dp \quad (c \in \mathbb{R}, c > 0). \quad (\text{A11})$$

We verify that (A11) is the inverse of (A10). Substituting the integrand in (A11) by the Laplace transform definition (A10) and pursuing some algebraic manipulations, we obtain:

$$\begin{aligned}
\chi(x, y) &= \frac{1}{2\pi i} \int_{c-i\infty}^{c+i\infty} dp e^{px} \int_0^{W/2} \chi(\hat{x}, y) e^{-p\hat{x}} d\hat{x} \\
&= \frac{1}{2\pi i} \int_0^{W/2} d\hat{x} \chi(\hat{x}, y) \int_{c-i\infty}^{c+i\infty} dp e^{p(x-\hat{x})} \\
&= \frac{1}{2\pi i} \int_0^{W/2} d\hat{x} \chi(\hat{x}, y) \int_{-i\infty}^{i\infty} i d\hat{p} e^{c(x-\hat{x})} e^{i\hat{p}(x-\hat{x})} \quad (\text{putting } p = c + i\hat{p}) \\
&= \frac{1}{2\pi} \int_0^{W/2} d\hat{x} e^{c(x-\hat{x})} \chi(\hat{x}, y) \int_{-\infty}^{\infty} d\hat{p} e^{i\hat{p}(x-\hat{x})},
\end{aligned}$$

that can be rewritten in terms of the Dirac-delta function  $\delta(x - \hat{x}) = \frac{1}{2\pi} \int_{-\infty}^{+\infty} e^{i\hat{p}(x-\hat{x})} d\hat{p}$ ,

$$\chi(x, y) = \frac{1}{2\pi} \int_0^{W/2} d\hat{x} e^{c(x-\hat{x})} \chi(\hat{x}, y) \delta(x - \hat{x}).$$

We resolve the integral to the right-hand-side and we finally recover the Airy function in the domain of our sheet ( $0 \leq x \leq W/2$ ) and zero otherwise.

The Laplace transformation of the bi-harmonic equation (A3) is

$$\begin{aligned}
p^4 f(y, p) + 2p^2 f_{,yy}(y, p) + f_{,yyyy}(y, p) &= p^3 \chi|_{x=0} + 2p^2 \chi_{,x}|_{x=0} - p \left[ -2\chi_{,yy}|_{x=0} + e^{-px} \chi_{,xx}|_{x=0}^{x=W/2} \right] \\
&\quad + 2\chi_{,yyx}|_{x=0} - e^{-px} \chi_{,xxx}|_{x=0}^{x=W/2}, \tag{A12}
\end{aligned}$$

where we have already substituted the BCs at  $x = W/2$  (A6b). Notice that we cannot infer all the boundary terms in the *rhs* of the equation solely from the Airy potential BCs (A6), and so we express the unknown functions with the aid of Fourier series. However, these terms should account for the stress singularities in the corners of a sheet when one edge is clamped and the other is free [24] (see Benthem [23] and Xin and Davidovitch [17] for a complete calculation of the stress singularities in the vicinity of a sheet corner with clamped-free edges). For  $\nu \sim 0.32$ ,  $\sigma_{\theta\theta}$  and  $\sigma_{\theta r}$  are given by [23]:

$$\sigma_{\theta\theta} \left( \theta = \frac{\pi}{2} \right) = c_1 r^{-1/4}, \quad \sigma_{r\theta} \left( \theta = \frac{\pi}{2} \right) = -c_2 r^{-1/4}, \tag{A13}$$

where  $c_1 = \sqrt{8 + 3\sqrt{7}} c_2$ , and  $c_2$  is a constant to be determined. Thus, in the corners of our sheet ( $x = 0, y = \pm 1$ ) we assume

$$\sigma_{xx}(x = 0, y \rightarrow \pm 1) = c_1 (1 \pm x)^{-1/4}, \tag{A14a}$$

$$\sigma_{xy}(x = 0, y \rightarrow \pm 1) = \mp c_2 (1 \pm x)^{-1/4}, \tag{A14b}$$

where the choice for the signs follows from the following discussion. When stretching longitudinally the transversely clamped edge ( $x = 0$ ), we exert a tension onto the sheet. By the action-reaction principle, we expect that the sheet responds to this tension with a compressive stress, and hence the sign difference in the  $\sigma_{xy}$  stress component. Along the transverse ( $x$ ) direction, the transverse clamp at  $x = 0$  prevents the Poisson effect — by which a longitudinal stretching induces transverse contraction —, and hence it exerts a transverse compression to which the sheet responds generating a tensile transverse stress ( $\sigma_{xx}(x = 0, y \rightarrow \pm 1) > 0$ ).

Hence, invoking the stress singularities at the corners (A14), we write

$$\chi_{,yy}|_{x=0} = \sigma_{xx}(0, y) = c_1 (1 - x)^{-1/4} + c_1 (1 + x)^{-1/4} - c_1 2^{-1/4} + \sum_m a_m \cos\left(\frac{m\pi}{2} y\right), \tag{A15a}$$

$$\chi_{,xy}|_{x=0} = -\sigma_{xy}(0, y) = c_2 (1 - x)^{-1/4} - c_2 (1 + x)^{-1/4} + c_2 2^{-1/4} y + \sum_n b_n \cos\left(\frac{n\pi}{2} y\right), \tag{A15b}$$

where  $a_m$  and  $b_n$  are yet to be determined constants, and  $m = 2k - 1, n = 2k$  for  $k \in \mathbb{Z}^+$ . We obtain from these the

remaining unknown functions in (A12):

$$\chi_{,xx}|_{x=0} = 1 + \nu \chi_{,yy}|_{x=0}, \text{ from (A6c)}, \quad (\text{A16a})$$

$$\chi_{,xyy}|_{x=0} = -\sigma_{xy,y}(0, y) = \frac{c_2}{4}(1-x)^{-5/4} + \frac{c_2}{4}(1+x)^{-5/4} + c_2 2^{-1/4} + \frac{\partial}{\partial y} \sum_n b_n \cos\left(\frac{n\pi}{2}y\right), \quad (\text{A16b})$$

$$\chi_{,xxx}|_{x=0} = -(2 + \nu)\chi_{,xyy}, \text{ from (A6c)}, \quad (\text{A16c})$$

$$\chi_{,x}|_{x=0} = \int dy \chi_{,xy}|_{x=0} + b_0 = b_0 - \frac{4}{3}c_2(1-x)^{3/4} - \frac{4}{3}c_2(1+x)^{3/4} + c_2 2^{-5/4}x^2 + \sum_n b_n \left(\frac{-2}{n\pi}\right) \cos\left(\frac{n\pi}{2}y\right), \quad (\text{A16d})$$

$$\chi|_{x=0} = \int dy \left( \int d\hat{y} \chi_{,\hat{y}}|_{x=0} + c_4 \right) + c_5 = c_5 + c_4 y + \frac{16}{21}c_1(1+x)^{7/4} - c_1 2^{-5/4}x^2 - \sum_m a_m \left(\frac{2}{m\pi}\right)^2 \cos\left(\frac{m\pi}{2}y\right), \quad (\text{A16e})$$

where  $c_4 = 0$ ,  $c_5 = c_1 \left(-\frac{16}{21}2^{7/4} + 2^{-5/4}\right)$  are computed using the BCs (A6a). Finally, we use the *cosine* Fourier series for  $\chi_{,xx}|_{x=W/2}$  and  $\chi_{,xxx}|_{x=W/2}$ ,

$$\chi_{,xx}|_{x=W/2} = \sum_m \alpha_m \cos\left(\frac{m\pi}{2}y\right), \quad (\text{A17a})$$

$$\chi_{,xxx}|_{x=W/2} = \sum_m \beta_m \cos\left(\frac{m\pi}{2}y\right), \quad (\text{A17b})$$

$m = 2k - 1$  for  $k \in \mathbb{Z}^+$ , where we exploited the symmetry in  $y$ , and we write the transformed bi-harmonic equation:

$$\begin{aligned} p^4 f(y, p) + 2p^2 f_{,yy}(y, p) + f_{,yyyy}(y, p) = & p^3 c_1 \left[ \frac{16}{21}(1-y)^{7/4} + \frac{16}{21}(1+y)^{7/4} - 2^{-5/4}y^2 + 2^{-5/4} - \frac{16}{21}2^{7/4} \right] \\ & + p^2 \left\{ c_2 \left[ -\frac{4}{3}(1-y)^{3/4} - \frac{4}{3}(1+y)^{3/4} + 2^{-5/4}y^2 \right] + b_0 \right\} \\ & + p \left\{ c_1(2 + \nu) \left[ (1-y)^{-1/4} + (1+y)^{-1/4} - 2^{-1/4} \right] + 1 \right\} \\ & - \nu c_2 \left[ \frac{1}{4}(1-y)^{-5/4} + \frac{1}{4}(1+x)^{-5/4} + 2^{-1/4} \right] \\ & - p^3 \sum_m a_m \left(\frac{2}{m\pi}\right)^2 \cos\left(\frac{m\pi}{2}y\right) - p^2 \sum_n b_n \frac{2}{n\pi} \cos\left(\frac{n\pi}{2}y\right) \\ & + p \left[ (2 + \nu) \sum_m a_m \cos\left(\frac{m\pi}{2}y\right) - e^{-pW/2} \sum_m \alpha_m \cos\left(\frac{m\pi}{2}y\right) \right] \\ & - \nu \frac{\partial}{\partial y} \sum_n b_n \sin\left(\frac{n\pi}{2}y\right) - e^{-pW/2} \sum_m \beta_m \cos\left(\frac{m\pi}{2}y\right), \quad (\text{A18}) \end{aligned}$$

$m = 2k - 1$ ,  $n = 2k$  for  $k \in \mathbb{Z}^+$ .

We solve this differential equation for  $f(y, p)$  and the corresponding BCs (A6a), which become

$$f(\pm 1, p) = 0; f_{,y}(y, p)|_{y=\pm 1} = 0, \quad (\text{A19})$$

we write the solution  $f(y, p)$

$$\begin{aligned} f(y, p) = & f_p(y, p) - \frac{2f_p(1, p)}{\sin 2p + 2p} [(\sin p + p \cos p) \cos py + (p \sin p)y \sin py] \\ & + \frac{2f_{p,y}(1, p)}{\sin 2p + 2p} [\sin p \cos py - (\cos p)y \sin py], \quad (\text{A20}) \end{aligned}$$

with the particular integral

$$\begin{aligned}
f_p(y, p) = & p^3 c_1 \frac{16}{21} \left\{ R \left[ \frac{7}{4}; p, -y \right] + R \left[ \frac{7}{4}; p, y \right] \right\} - p^2 c_2 \frac{4}{3} \left\{ R \left[ \frac{3}{4}; p, -y \right] + R \left[ \frac{3}{4}; p, y \right] \right\} \\
& + p c_1 (2 + \nu) \left\{ R \left[ \frac{-1}{4}; p, -y \right] + R \left[ \frac{-1}{4}; p, y \right] \right\} - \frac{1}{4} \nu c_2 \left\{ R \left[ \frac{-5}{4}; p, -y \right] + R \left[ \frac{-5}{4}; p, y \right] \right\} \\
& + \frac{2^{-5/4}}{p^4} (-p c_1 + c_2) (y^2 p^2 - 4) - \frac{2^{-1/4}}{p^4} \nu c_2 + \frac{1}{p^3} [-2^{-1/4} c_1 (2 + \nu) + 1] \\
& + \frac{1}{p^2} b_0 + \frac{1}{p} c_1 \left( 2^{-5/4} - \frac{16}{21} 2^{7/4} \right) + \sum_m \frac{a_m \left[ -p^3 \left( \frac{2}{m\pi} \right)^2 + p(2 + \nu) \right] - e^{-pW/2} (p \alpha_m + \beta_m)}{\left[ p^2 - \left( \frac{m\pi}{2} \right)^2 \right]^2} \cos \left( \frac{m\pi}{2} y \right) \\
& - \sum_n b_n \frac{p^2 \frac{2}{n\pi} + \nu \frac{n\pi}{2}}{\left[ p^2 - \left( \frac{n\pi}{2} \right)^2 \right]^2} \cos \left( \frac{n\pi}{2} y \right), \tag{A21}
\end{aligned}$$

$m = 2k - 1$ ,  $n = 2k$  for  $k \in \mathbb{Z}^+$ ; where, to express this more compactly, we defined an ‘auxiliary’ function  $R[q; p, y]$ :

$$R[q; p, \pm y] \equiv \frac{1}{2p^3} \int_0^y (1 \pm \xi)^q \sin p(y - \xi) d\xi - \frac{1}{2p^2} \int_0^y (1 \pm \xi)^q (y - \xi) \cos p(y - \xi) d\xi. \tag{A22}$$

To obtain the Airy potential,  $\chi(x, y)$ , we compute the inverse Laplace transform (A11) of the function  $f(y, p)$  (A20). To calculate the line integral (A11), we define a closed contour  $\mathcal{C}$  in the complex plane and then apply the Residue Theorem [25]. Note that, for arbitrary values of  $(c_1, b_0, a_m, b_n, \alpha_m, \beta_m)$ , the function  $f(y, p)$  has poles at  $p = p_k$ , where  $p_k$  are the (complex) roots of the trigonometric equation (A8) ( $p_k \neq 0$ ) — the double poles at  $p = \pm n\pi/2$ ,  $p = \pm m\pi/2$ , and the pole at  $p = 0$  can be removed. Thus, in order that the integral (A11) converges we need these poles at  $p = p_k$  to be removed, *i.e.* their residues to vanish

$$\text{Res}[f(y, p), p = p_k] = \frac{1}{2} [f_{p,y}(y, p_k)|_{y=1} - \sin^2 p_k f_p(1, p_k)] \frac{[\sin p_k \cos p_k y - (\cos p_k) y \sin p_k y]}{\cos^2 p_k} = 0. \tag{A23}$$

This leads to an infinite system of algebraic equations in the unknowns  $(c_1, b_0, a_m, b_n, \alpha_m, \beta_m)$ . Following the calculation of Benthem [23], we take only a finite number of unknowns — *i.e.* we truncate the Fourier series in the particular integral (A21) —; the sufficient number of equations to calculate  $(c_1, b_0, a_m, b_n, \alpha_m, \beta_m)$  is then obtained by using the necessary number of values of  $p_k$  (ordered by increasing real part). Substituting the numerical values of  $(c_1, b_0, a_m, b_n, \alpha_m, \beta_m)$  into the particular integral (A21), we obtain a function  $f(y, p)$  that has no poles, and thus whose complex line integral (A11) converges.

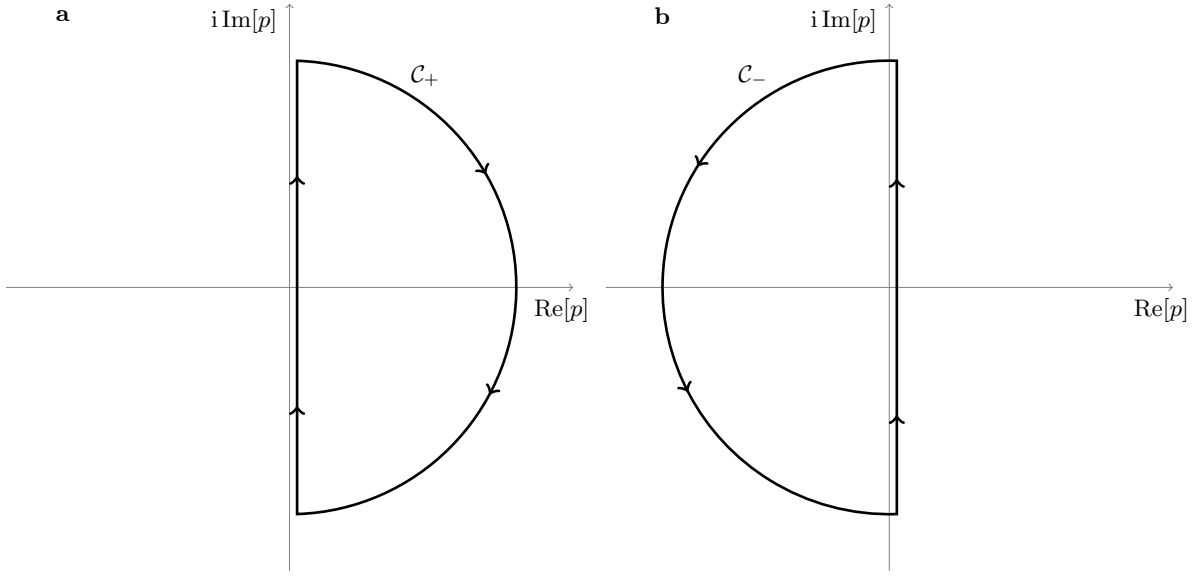
So far our discussion has focused on the function  $f(y, p)$ , yet we notice that it multiplies the exponential  $e^{px}$  in the inverse Laplace formula (A11). We close the integration contour so that  $f(y, p)e^{px}$  is an analytic function, continuous within  $\mathcal{C}$ . Hence, by writing  $f(y, p)$  as

$$f(y, p) = e^{-pW/2} f_+(y, p) + f_-(y, p), \tag{A24a}$$

$$\begin{aligned}
\text{with } f_+(y, p) = & \sum_m \frac{(p\alpha_m + \beta_m)}{\left[ p^2 - \left( \frac{m\pi}{2} \right)^2 \right]^2} \left[ -\cos \left( \frac{m\pi}{2} y \right) \right. \\
& \left. + m\pi \sin \left( \frac{m\pi}{2} \right) \frac{[\sin p \cos py - (\cos p) y \sin py]}{\sin 2p + 2p} \right], \tag{A24b}
\end{aligned}$$

$$\text{and } f_-(y, p) = f(y, p) - e^{-pW/2} f_+(y, p), \tag{A24c}$$

$m = 2k - 1$  for  $k \in \mathbb{Z}^+$ , and substituting this into the integral (A11), we find that the integration line must be closed in either of the contours  $\mathcal{C}_\pm$  in Fig. A9 for the integral of each term. Note that the functions  $f_\pm(y, p)$  in (A24) have poles at  $p = p_k$ . Applying the Residue Theorem [25] (or Cauchy’s Theorem in those cases for which the integrand is



Extended Data Fig. A9. **Contours in the complex plane a-b.**

$f(y, p)e^{px}$ , we find that

$$\chi(x, y) = \begin{cases} \frac{1}{2\pi i} \oint_{C_+} f(y, p)e^{px} dp = 0, & \text{for } x < 0, \\ \frac{1}{2\pi i} \oint_{C_+} f_+(y, p)e^{p(x-W/2)} + \oint_{C_-} f_-(y, p)e^{px} dp = \\ \quad - \sum_k e^{p_k(x-W/2)} \text{Res}[f_+(y, p_k), \text{Re}[p_k] > 0] + \sum_k e^{p_k x} \text{Res}[f_-(y, p_k), \text{Re}[p_k] < 0], & \text{for } 0 \leq x \leq W/2 \\ \frac{1}{2\pi i} \oint_{C_-} f(y, p)e^{px} dp = 0, & \text{for } x > W/2. \end{cases} \quad (\text{A25})$$

Note the different signs in the two terms in the Airy potential within the sheet domain ( $x \in [0, W/2]$ ); "a closed contour is described in a positive direction with respect to the domain enclosed by the contour if with respect to some point inside the domain the contour is traversed in a counterclockwise direction" [25].

It is only a matter of some (tedious) algebra to calculate the residues in (A25) (using (A23) and the corresponding definitions of the functions  $f_{\pm}(y, p)$  (A24)). Finally, we obtain the result in (A7), with

$$C_k = - \frac{\sin p_k}{\cos^2 p_k} \sum_m \frac{(p_k \alpha_m + \beta_m)}{\left[p_k^2 - \left(\frac{m\pi}{2}\right)^2\right]^2} m\pi \sin\left(\frac{m\pi}{2}\right), \quad (\text{A26a})$$

$$\hat{C}_k = - [f_{p,y}^{(-)}(1, -p_k) - \sin^2 p_k f_p^{(-)}(1, -p_k)] \frac{\sin p_k}{\cos^2 p_k}, \quad (\text{A26b})$$

$m = 2k - 1$  for  $k \in \mathbb{Z}^+$ ; where, to write things more compactly, we have introduced the function  $f_p^{(-)}(y, p)$

$$f_p^{(-)}(y, p) = f_p(y, p) + e^{-pW/2} \sum_m \frac{(p \alpha_m + \beta_m)}{\left[p^2 - \left(\frac{m\pi}{2}\right)^2\right]^2} \cos\left(\frac{m\pi}{2} y\right). \quad (\text{A27})$$

### 3. Near-threshold analysis

Based on the planar stress field results discussed previously, we examine the buckling of a clamped square sheet, of side  $\sim W$  and thickness  $t$ , subject to a uniform bi-axial stress field of modulus  $\sim T$ , which is tensile along the  $y$  axis,  $\sigma_{yy} \sim T$ , and compressing the  $x$  axis,  $\sigma_{xx} \sim -T$ .

We assume then an undulating displacement field  $\zeta(x, y) = \delta \cdot g_\lambda(x, y)$ . The amplitude  $\delta$  is infinitesimal and  $g_\lambda(x, y)$  is some undulating function along the compressive axis with a characteristic length  $\lambda$ , yet unknown. Along the tensile axis,  $g_\lambda(x, y)$  simply suppresses the amplitude at the edges  $\pm W/2$ . The excess bending energy associated with this perturbation is  $U_{\text{bend}} \sim B \int (\nabla^2 \zeta)^2 dA \sim B W^2 \left[ \left( \frac{\delta}{\lambda^2} \right)^2 + \left( \frac{\delta}{W^2} \right)^2 \right]$  — the full sheet width at the edges is clamped, and hence going out of plane effectively means that the sheet develops a non-zero curvature along both the tensile and the compressing directions. For a given  $\lambda$ , the excess stretching energy of this double curvature is  $U_{\text{stretch}} \sim \int \sigma : \epsilon dA \sim T W^2 \delta^2 / W^2 - \sigma_{xx}(\lambda) W^2 \delta^2 / \lambda^2$ , and hence the planar state becomes unstable only if the compressive load exceeds

$$\sigma_{xx}(\lambda) \sim \frac{B}{\lambda^2} + \left( \frac{B}{W^4} + \frac{T}{W^2} \right) \lambda^2. \quad (\text{A28})$$

However, since  $\sigma_{xx}$  is also proportional to  $T$ , we find that

$$T \sim \frac{B}{\lambda^2} \frac{\left( 1 + \frac{\lambda^4}{W^4} \right)}{\left( 1 + \frac{\lambda^2}{W^2} \right)}. \quad (\text{A29})$$

Since the wavelength is limited by  $W$ , we express  $\lambda$  as  $\lambda = \xi W$ , with  $\xi \in (0, 1]$ ; then we can write  $T \sim \frac{B}{W^2} g(\xi)$ , with  $g(\xi) = \frac{1}{\xi^2} \frac{(1+\xi^4)}{(1+\xi^2)}$ . For  $\xi \ll 1$ ,  $g(\xi) \sim \xi^{-2} > 1$ ; while for  $\xi \sim 1$  (*i.e.*  $\xi = 1 - \varepsilon$ ,  $\varepsilon \ll 1$ ),  $g(\xi) \sim (1 - \varepsilon)^{-2} > 1$ . Thus, we have that  $g(\xi < 1) > 1$  and  $g(\xi = 1) = 1$ ; or, in other words,  $g(\xi = 1) = 1$  is the minimum value of  $g(\xi)$  in the interval  $\xi \in (0, 1]$ . This minimum gives the threshold value for the tension

$$T_c \sim \frac{B}{W^2}. \quad (\text{A30})$$

In terms of the longitudinal in-plane end-stretching imposed,  $\epsilon_{\text{planar}}$ , we conclude that the end-stretched sheet buckles when the longitudinal in-plane displacement  $\epsilon_{\text{planar}}$  exceeds  $\epsilon_c$ , with

$$\epsilon_c \sim \frac{B}{Y W^2}. \quad (\text{A31})$$